# Origami Metamaterials for Tunable Thermal Expansion

*Elisa Boatti, Nikolaos Vasios, and Katia Bertoldi**

**Materials with engineered thermal expansion, capable of achieving targeted area/volume changes in response to variations in temperature, are important for a number of aerospace, optical, energy, and microelectronic applications. While most of the proposed structures with engineered coefficient of thermal expansion consist of bi-material 2D or 3D lattices, here it is shown that origami metamaterials also provide a platform for the design of systems with a wide range of thermal expansion coefficients. Experiments and simulations are combined to demonstrate that by tuning the geometrical parameters of the origami structure and the arrangement of plates and creases, an extremely broad range of thermal expansion coefficients can be obtained. Differently from all previously reported systems, the proposed structure is tunable in situ and nonporous.**

From engines, buildings, and solar energy systems to lenses, space crafts, and tooth fillings, many systems require components capable of achieving targeted area/volume changes in response to variations in temperature.[1–6] While some of them (including bearings and structures with high tolerances) benefit from materials whose area/volume is unaltered by changes in temperature, others (such as piping connections and tooth fillings) require materials that match the thermal expansion of the surrounding environment.

Motivated by these needs, two main strategies have been proposed to create components capable of achieving a wide range of coefficients of thermal expansion, from extremely negative, through zero, to largely positive. On the one hand, it has been shown that the coefficient of thermal expansion can be controlled by exploiting supramolecular mechanisms, such as ferroelectric, magnetostrictive and displacive phase transitions, low-frequency phonon modes, and rigid unit modes.[2] However, the resulting materials typically possess characteristics that limit their use in applications demanding robustness and durability over large temperature changes. On the other hand, coefficients of thermal expansion outside the range attainable with conventional materials have been achieved by carefully designing the architecture of structures made of multiple constituents. However, the proposed architected materials, which include 2D[6–10] and 3D[11–15] multimaterials lattices as well as bi-materials microstructures,[16,17] are all porous and characterized by a response that is very difficult to be tuned after manufacturing.

Origami—the ancient art of paper folding—not only leads to aesthetically pleasant structures but also enables the design of materials with novel mechanical properties, including negative and adjustable Poisson's ratio,[18–21] programmable curvature[22] and mechanical response,[23] and multistability.[24] Here, we focus on a simple origami tessellation, the Miura-ori,[25] and combine experiments with simulations to demonstrate that this system can also provide a platform for the design of materials with a wide range of coefficients of thermal expansion. To achieve this goal, we introduce into the tessellation bilayer faces, which undergo a bending deformation upon changes in temperature. Our results indicate that a careful choice of the bilayer facets location and of the creases stiffness can produce a variety of qualitatively very different responses upon variations in temperature. Moreover, we demonstrate that folding of the Miura-ori enables in situ tunability of the coefficient of thermal expansion, opening avenues for the design of a new class of nonporous systems whose thermal properties can be adapted to the surrounding environment.

To illustrate this concept, we focused on a Miura-ori fabricated from paper (Boise ASPEN 30, 92 Brightness, 20 lb, 11 × 17 in.), with Young's modulus $E_{paper}$ = 4700 MPa, coefficient of thermal expansion $\alpha_{paper} = 2 \times 10^{-6}$ K$^{-1}$ and thickness $t_{paper}$ = 0.1 mm, and adhesive-backed ultra-high molecular weight (UHMW) polyethylene film (McMaster-Carr identification number 1441T12), with $E_{PE}$ = 400 MPa, $\alpha_{PE} = 1.3 \times 10^{-4}$ K$^{-1}$, and $t_{PE}$ = 0.127 mm (see the Supporting Information for details). The proposed Miura-ori (see schematic in **Figure 1**a) is comprised of both single-layer (white) and bilayer (gray) plates, connected through a combination of soft (green) and stiff (red) creases. The single-layer facets are made purely of paper, while the bilayer ones include a paper bottom layer and a polyethylene top layer, glued together. Similarly, the soft creases are made of paper only, while the stiff ones comprise paper and polyethylene film. We started by investigating the response of three different Miura-ori structures, all presenting parallelogram facets with sides $a = b$ = 30 mm and acute angle $\beta$ = 60°. Design #A is comprised of only bilayer plates, all connected by soft creases (see Figure 1b). Differently, designs #B and #C include an identical number of single-layer and bilayer plates and present all soft creases except some of those connecting the

Dr. E. Boatti, N. Vasios
John A. Paulson School of Engineering and Applied Science
Harvard University
Cambridge, MA 02138, USA
Prof. K. Bertoldi
Kavli Institute
Harvard University
Cambridge, MA 02138, USA
E-mail: bertoldi@seas.harvard.edu

**DOI: 10.1002/adma.201700360**



© 2017 WILEY-VCH Verlag GmbH & Co. KGaA, Weinheim

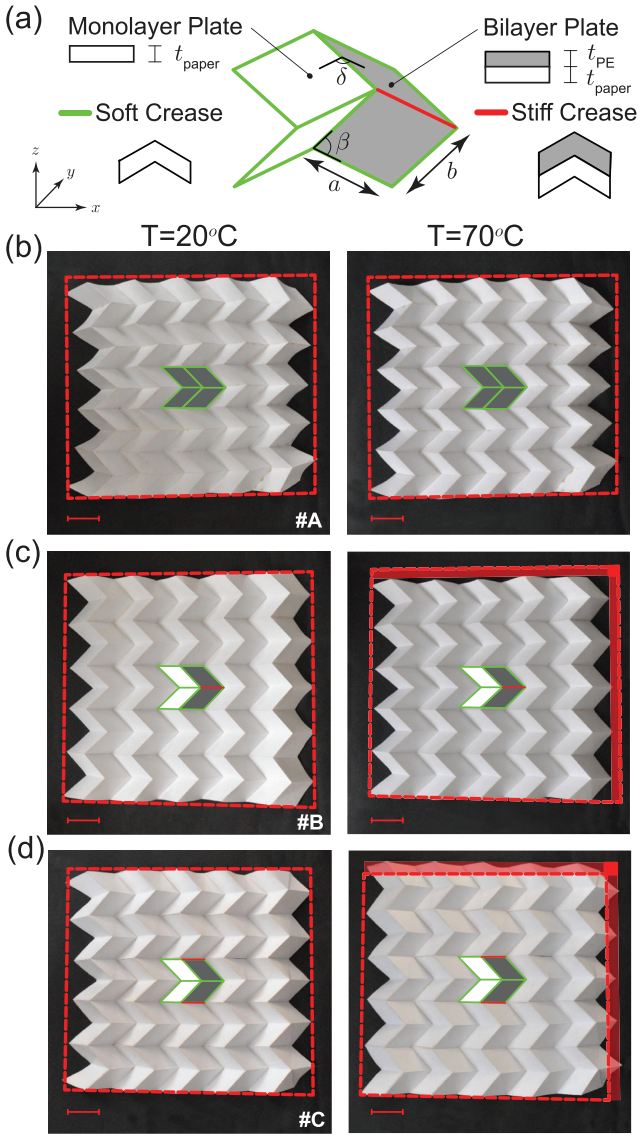


**Figure 1.** Origami metamaterials for tunable coefficient of thermal expansion. a) Schematic of the unit cell of the considered origami metamaterial. The structure is comprised of both single-layer (white) and bilayer (gray) plates, connected by a combination of soft (green) and stiff (red) creases. Top views of samples b) #A, c) #B, and d) #C at 20 °C (left) and at 70 °C (right). For each structure, a schematic of the unit cell is highlighted in the center of the sample. The red dashed box indicates the projected area of the sample at 20 °C. (Scale bars: 30 mm).

bilayer plates. More specifically, in design #B the stiff creases are located on the mountains between the bilayers (see Figure 1c), while in #C they are on the valleys between them (see Figure 1d).

Samples composed of 5 × 5 unit cells were manufactured by laser-cutting the pattern of creases into both the paper and the polyethylene sheets, which were subsequently glued together (see the Supporting Information for further fabrication details). Finally, the Miura-ori were manually folded so that their opening angle was $\delta \approx 70°$ and heated uniformly by placing them in an oven (model 414004-580 VWR) and slowly increasing the temperature by $\Delta T = 50$ °C. In Figure 1 we report snapshots of the three structures taken before and after heating and we indicate with a red dashed box the projected area of the samples at room temperature. Surprisingly, we find that the three considered Miura-ori respond very differently to the increase in temperature. Design #A does not display a visible change in area upon heating (Figure 1b). Differently, structure #B considerably shrinks (Figure 1c) and design #C significantly expands (Figure 1d).

The response of the three structures upon heating can be characterized by calculating the effective coefficients of thermal expansion along both the $x$ and $y$-directions. To minimize the influence of edge effects, we focused on four unit cells in the center of the sample and calculated $\bar{\alpha}_x$ and $\bar{\alpha}_y$ as (see the Supporting Information for details)

$$\bar{\alpha}_x = \left\langle \alpha_x^{[i,j]} \right\rangle = \left\langle \frac{\Delta x^{[i,j]}}{L_x^{[i,j]} \Delta T} \right\rangle$$
$$\bar{\alpha}_y = \left\langle \alpha_y^{[i,j]} \right\rangle = \left\langle \frac{\Delta y^{[i,j]}}{L_y^{[i,j]} \Delta T} \right\rangle \quad (1)$$

where $\Delta x^{[i,j]}$ and $\Delta y^{[i,j]}$ denote the change in size of the $[i, j]$ th unit cell along the $x$ and $y$-directions, respectively; moreover, $L_x^{[i,j]}$ and $L_y^{[i,j]}$ are the initial dimensions of the unit cell along $x$ and $y$ (see the inset in **Figure 2**b), and $\langle \cdot \rangle$ indicates the average operation. For the configurations of designs #A, #B, and #C shown in Figure 1 we found that the normalized thermal expansion coefficients are $(\bar{\alpha}_x/\alpha_{PE}; \bar{\alpha}_y/\alpha_{PE}) = (-1.4; -2.1)$, $(-4.6; -6.0)$, and $(9.3; 7.4)$, respectively.

Since our origami structures are foldable, we repeated the experiments for different opening angles $\delta$. The experimental results shown as markers in Figure 2a,b reveal an important feature of our system: the coefficient of thermal expansion can be tuned in situ by varying the opening angle. More specifically, we find that, for the $\delta$ range considered, the shrinkage and expansion of designs #B and #C tend to progressively decrease as the opening angle $\delta$ increases. This marks a difference with previously proposed concepts, whose response is characterized by fixed coefficients of thermal expansion, that are typically extremely difficult to tune and control after the assembly.[6,14,15] Finally, we note that $\delta$ has almost no effect on design #A, which is always characterized by negligible area changes.

To better understand the behavior of our origami structures, we investigated their response through numerical simulations conducted with the finite element code Abaqus/Standard. In all our simulations we considered a unit cell with suitable periodic boundary conditions applied to its edges.[26] 3D models were constructed using quadratic six-noded shell elements and the bilayer plates were simulated by building a composite stack and assigning the appropriate material parameters to each layer. The mechanical response of the paper and polyethylene sheets was captured using linear elastic models with Young's modulus $E_{paper}$ and $E_{PE}$, Poisson's ratio $\nu_{paper} = \nu_{PE} = 0.3$, and coefficients of thermal expansion $\alpha_{paper}$ and $\alpha_{PE}$. Moreover, the behavior of the soft and stiff creases was captured by connecting neighboring plates through linear rotational springs with stiffness $k_{soft}$ or $k_{stiff}$, respectively. Note that the stiffness of the soft and stiff creases was characterized experimentally by testing


© 2017 WILEY-VCH Verlag GmbH & Co. KGaA, Weinheim

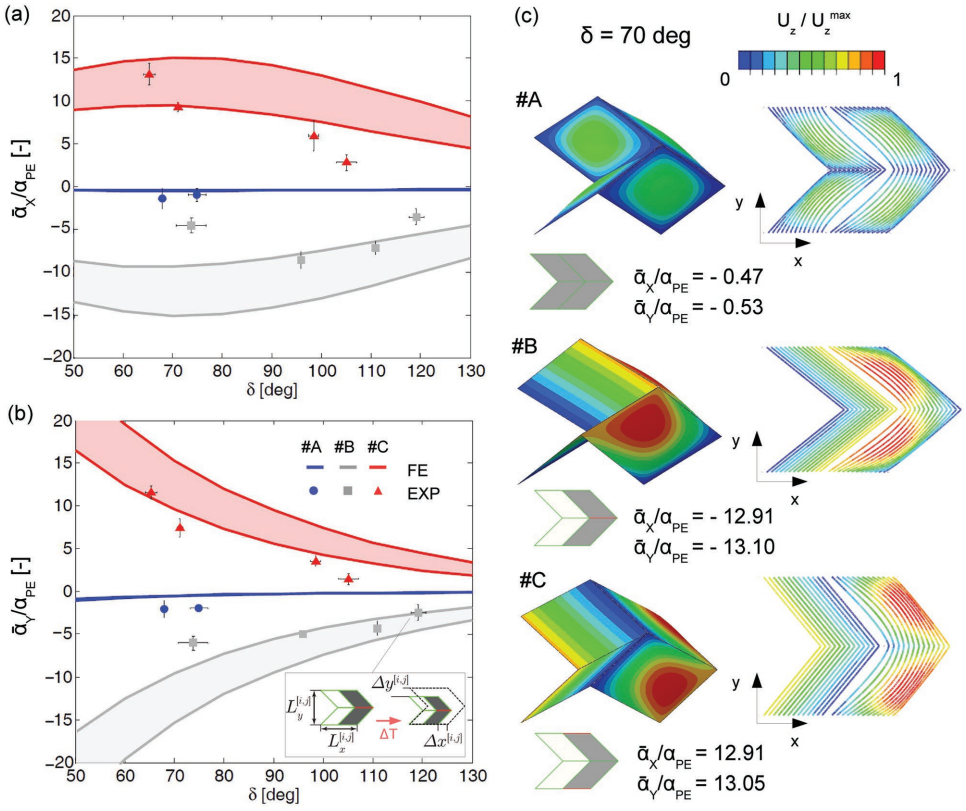


**Figure 2.** Experimental and numerical results. Comparison of experimental and numerical results for a) $\bar{\alpha}_x/\alpha_{PE}$ and b) $\bar{\alpha}_y/\alpha_{PE}$. The inset at the bottom of (b) shows a schematic of a Miura-ori unit cell with the initial dimensions and the change in size upon heating; these quantities have been used in the postprocessing of the experimental data to derive the effective thermal expansion coefficients of the samples (see Equation (1)). c) Rotated and top views of the numerical deformed configuration for designs #A, #B, and #C. These models are characterized by $\delta = 70°$, $k_{soft} = 0.0021$ N rad$^{-1}$, and $k_{stiff}/k_{soft} = 10.3$. For each of the three cases, the obtained values of $\bar{\alpha}_x/\alpha_{PE}$ and $\bar{\alpha}_y/\alpha_{PE}$ are reported.

rectangular plates connected by three folds (see the Supporting Information for more details). We found that the response of the creases can be modeled using linear rotational springs with stiffness $k_{soft} = 0.0021 \pm 0.0003$ N rad$^{-1}$ and $k_{stiff} = 0.0205 \pm 0.0055$ N rad$^{-1}$. These results clearly show that the stiff creases are one order of magnitude stiffer than the soft ones. Moreover, they also indicate that there is non-negligible variability in the creases stiffness, since their response is highly affected by the way they are manually folded—a process that is very difficult to precisely control. As such, to take this into account, in our simulations we considered $k_{soft} \in [0.0018, 0.0024]$ and $k_{stiff} \in [0.015, 0.026]$. Finally, the numerical effective coefficients of thermal expansion in the $x$ and $y$-directions were calculated from the macroscopic strains $\bar{\varepsilon}_{xx}$ and $\bar{\varepsilon}_{yy}$ of the Miura-ori unit cell as

$$\bar{\alpha}_x = \frac{\bar{\varepsilon}_{xx}}{\Delta T}, \quad \bar{\alpha}_y = \frac{\bar{\varepsilon}_{yy}}{\Delta T} \tag{2}$$

In Figure 2a,b we report as shaded areas the numerical predictions for $\bar{\alpha}_x$ and $\bar{\alpha}_y$ as a function of the opening angle $\delta$ for the considered ranges of $k_{stiff}$ and $k_{soft}$. The numerical results show an overall agreement with the experimental ones and confirm that changes in the opening angle can be exploited to in situ tune $\bar{\alpha}$. Note that the discrepancies between numerical and experimental results are due to the difficulties in controlling and measuring the creases stiffness with current materials and manufacturing procedure.

Further understanding into the mechanisms resulting in the different responses of designs #A, #B, and #C can be obtained by inspecting the numerical snapshots of the three heated structures. In Figure 2c we report the deformed configuration for the three considered Miura-ori designs characterized by $\delta = 70°$, $k_{stiff}/k_{soft} = 10.3$, and $k_{soft} = 0.0021$ N rad$^{-1}$. It can be noted that, as expected, all bilayer plates bend and take a dome-like shape upon the increase in temperature. However, while in design #A (with all soft creases) such bending minimally affects the opening angle of the creases, in structures #B and #C it forces the soft creases to significantly close and open, respectively, triggering a change in the area occupied by the Miura-ori upon heating. Therefore, we can conclude that the large coefficients of thermal expansion of designs #B and #C are driven by the stiff creases, which are strong enough to resist changes in their opening angle and to force the soft creases to significantly open/close.

Next, to better understand the role of the soft/stiff creases and of the monolayer/bilayer plates arrangement, we numerically explored the response upon heating of Miura-ori structures characterized by $a/b = 1$, $\beta = 60°$, $\delta = 70°$, and different arrangements of $k_{soft}$, $k_{stiff}$, and monolayer/bilayer facets. Note


© 2017 WILEY-VCH Verlag GmbH & Co. KGaA, Weinheim

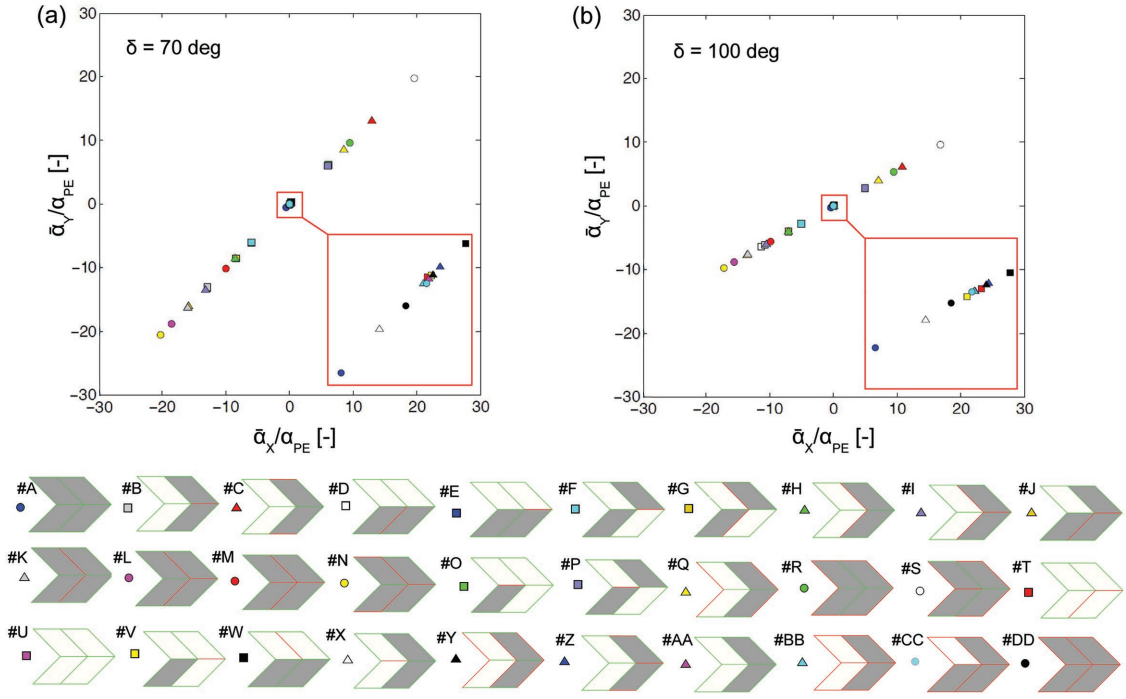


**Figure 3.** Effect of creases and plates arrangement. Numerical predictions of $\bar{\alpha}_x$ and $\bar{\alpha}_y$ for different arrangements of the bilayer plates and of the soft and stiff creases. A magnification of the numerical results around the origin of the axes is shown on the bottom right of the plots. Results are reported for a) $\delta = 70°$ and b) $\delta = 100°$.

that for this set of simulations we used $k_{stiff}/k_{soft} = 10.3$ and $k_{soft} = 0.0021$ N rad$^{-1}$. The results reported in **Figure 3** indicate that negative values of thermal expansion are achieved in the presence of bilayer facets when the stiff creases are located prevalently on mountains (see designs #B and #D–#N). We also find that by moving the stiff creases from mountains to valleys, the coefficients of thermal expansion change from negative to positive values (see designs #C and #O–#S). Moreover, our simulations show that to maximize $|\bar{\alpha}|$ the stiff creases need to be arranged between bilayer plates. Differently, small effective coefficients of thermal expansion, comparable with $\alpha_{paper}$, are observed when either all plates are single-layer (see designs #T and #U), or the stiff creases connect single-layer facets (see designs #V–#X) or the stiff creases are located evenly on mountains and valleys (because of their contrasting effect on $\bar{\alpha}$; see designs #Y and #Z), or all creases are identical (see designs #A and #AA–#DD). Additionally, it is worth pointing out that the ratio $\bar{\alpha}_y/\bar{\alpha}_x$ is controlled by the geometrical parameters, while it is independent on the arrangement of the bilayer plates and of the soft and stiff creases. As a result, all the points in Figure 3a lay on a straight line, whose slope can be controlled by changing the geometry of the structure. As an example, in Figure 3b we report the coefficients of thermal expansion for identical structures, but with opening angle $\delta = 100°$. By changing $\delta$ from 70° to 100° we find that $\bar{\alpha}_y/\bar{\alpha}_x$ varies from 1.01 to 0.57 (see the Supporting Information for additional results). Finally, it should be noted that the configurations considered in Figure 3 that comprise stiff creases between monolayers or between a bilayer and a monolayer are extremely difficult to be realized experimentally with the materials and fabrication procedure used in this study. However, they have been included to offer a more complete picture of the responses that can be achieved with the proposed concept.

While the results reported in Figures 1, 2, 3 are all for a Miura-ori characterized by $a/b = 1$ and $\beta = 60°$, further tunability can be achieved by altering the geometry of the structure. In **Figure 4** we report as contour plots the evolution of $\bar{\alpha}_x/\alpha_{PE}$ and $\bar{\alpha}_y/\alpha_{PE}$ as a function of the angles $\beta$ and $\delta$ for two different geometries characterized by $a/b = 1$ and $a/b = 5$. Our results indicate that the facets aspect ratio $a/b$ does not affect the distribution of $\bar{\alpha}_x$ and $\bar{\alpha}_y$ as a function of $\beta$ and $\delta$, but only changes their magnitude. Moreover, we find that the most negative values of $\bar{\alpha}_x$ can be achieved for large acute angles $\beta$ and small opening angles $\delta$, while large negative values of $\bar{\alpha}_y$ are achieved for small $\delta$ and intermediate values of $\beta$. Finally, we note that also the Young's moduli, thermal expansion coefficients, and thicknesses of the two layers affect the macroscopic thermal response of the Miura-ori, with the Young's moduli and the layers thickness also influencing the stiffness of the creases (see the Supporting Information for details).

Our combined experimental and numerical results indicate that by varying the bilayers and creases arrangement and by altering the geometry of the Miura-ori, qualitatively very different responses can be achieved upon changes in temperature. However, for practical applications it is very important to be able to easily identify configurations resulting in specific values of the coefficients of thermal expansion. Such a problem can be expressed as a numerical optimization problem whose solution is the set of input parameters that minimize


© 2017 WILEY-VCH Verlag GmbH & Co. KGaA, Weinheim

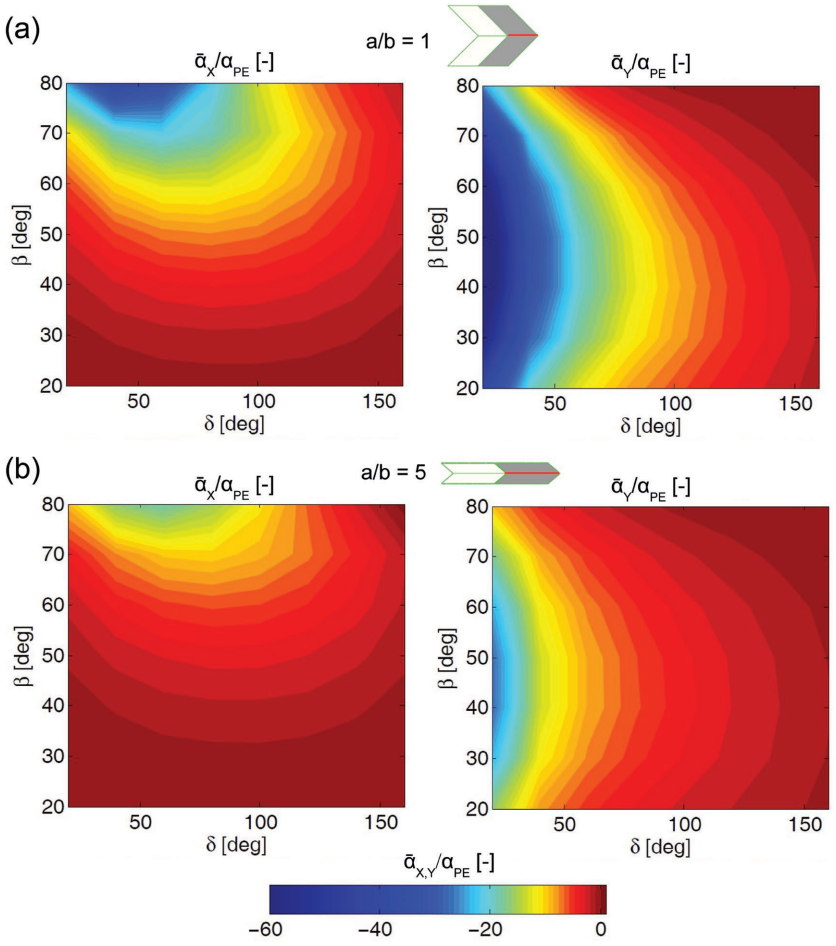


**Figure 4.** Effect of geometry. Contour plots showing the distribution of $\bar{\alpha}_x/\alpha_{PE}$ (left) and $\bar{\alpha}_y/\alpha_{PE}$ (right) as a function of the angles $\beta$ and $\delta$. Numerical results for a) $a/b = 1$ and for b) $a/b = 5$ are reported.

a prescribed objective function.[27] For the considered origami structures, the objective function $Z$ can be defined in terms of the in-plane thermal expansion coefficients $\bar{\alpha}_x$ and $\bar{\alpha}_y$, whereas the input parameters to that objective function are taken to be the acute angle $\beta$, the opening angle $\delta$, and the ratio of lengths of the parallelogram facets $a/b$ (note that to avoid excessive complexity in the calculations, we considered in every optimization problem a fixed arrangement of plates and creases). The optimization problem was solved using the COBYLA algorithm,[28] which is a gradient-free algorithm that uses linear approximations to the objective and constraint functions and is suitable for nonlinear constrained optimization problems with low dimensionality. For each evaluation of the objective function, a numerical simulation using Abaqus/Standard was conducted to derive $\bar{\alpha}_x$ and $\bar{\alpha}_y$ for the set of inputs $\beta$, $\delta$, and $a/b$ determined by COBYLA. Note that the input parameters were constrained as $\beta \in [10, 90]°$, $\delta \in [20, 160]°$, and $(a/b) \in [0.2, 2]$ to make sure that the resulting Miura-ori configuration was always well defined. In **Figure 5** we report results for two different cases that are of particular interest for applications. First, we determined the optimal Miura-ori geometry resulting in the most negative pair of identical coefficients of thermal expansion along the $x$ and $y$-directions. To this end, we minimized the following objective function

$$Z = \left(\bar{\alpha}_x + \bar{\alpha}_y\right) \cdot \left[1 + 0.5\left|\bar{\alpha}_x - \bar{\alpha}_y\right|\right]^{-1} \tag{3}$$

using the arrangement of plates and creases of configuration #N, since the results of Figure 3 indicate that this design is a reasonably good candidate to achieve the target. As shown in Figure 5a, after 44 iterations the algorithm finds the most negative pair of $\bar{\alpha}_x$, $\bar{\alpha}_y$ that simultaneously satisfies the condition $\bar{\alpha}_x = \bar{\alpha}_y$ for $\beta = 62.73°$, $\delta = 62.10°$, and $a/b = 0.689$. In fact, for this set of geometric parameters, we obtain $\bar{\alpha}_x/\alpha_{PE} = \bar{\alpha}_y/\alpha_{PE} = -26.40$. Second, we were interested in a Miura-ori geometry characterized by $|\bar{\alpha}_x|$ and $|\bar{\alpha}_y|$ both ≈0. To identify this configuration, we minimized

$$Z = -\left[\left|\bar{\alpha}_x\right| + \left|\bar{\alpha}_y\right| + 10^8\left(\bar{\alpha}_x^2 - \bar{\alpha}_y^2\right)^2\right]^{-1/4} \tag{4}$$

and, guided by the results of Figure 3, considered the arrangement of plates and creases of configuration #AA. As shown in Figure 5b, we find that for $\beta = 53.69°$, $\delta = 111.21°$, and $a/b = 0.68$ we achieve $\bar{\alpha}_x/\alpha_{PE} = 0.0009$ and $\bar{\alpha}_y/\alpha_{PE} = -0.0007$. It is important to point out that such $|\bar{\alpha}|$ values are lower than the thermal expansion coefficient of the paper (in fact, $\alpha_{paper}/\alpha_{PE} = 0.015$).

In conclusion, we have combined experiments and simulations to demonstrate that origami metamaterials provide a new platform for the design of systems with a wide range of coefficients of thermal expansion. In particular, we have shown that by controlling the arrangement of single and bilayer facets, the stiffness of the creases, and the geometric parameters, we can achieve a variety of qualitatively different responses upon variations in temperature. The structure proposed here presents two main differences with respect to existing systems: first, it is possible to tune its thermal response in situ simply by changing the opening angle $\delta$, without the need to fabricate a new structure; second, it is intrinsically nonporous and therefore can be preferred in applications where a separation between two regions is required. Additionally, while here we focused on structures at centimeter scale made of paper and polyethylene, the proposed design can be potentially extended to different materials and length scales. As such, our study provides new opportunities for the design of materials and components capable of achieving extreme and customizable thermal expansion properties that can be of particular interest for applications in aerospace,[4,29] optics,[6,30] energy,[1,3,31] and microelectronics.[5,32]


© 2017 WILEY-VCH Verlag GmbH & Co. KGaA, Weinheim

Received: January 18, 2017
Revised: March 6, 2017
Published online:

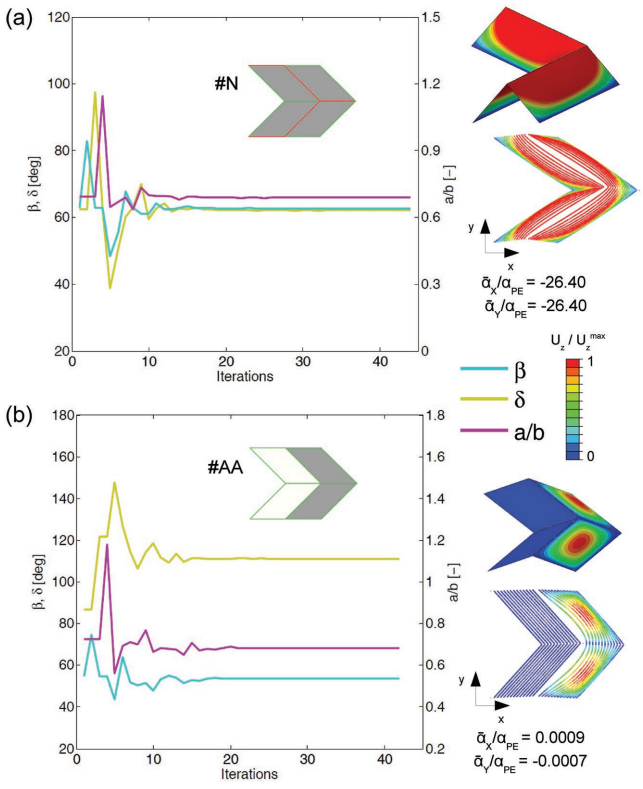


**Figure 5.** Optimization. An optimization algorithm is used to identify the Miura-ori configuration for which $\bar{\alpha}_x/\alpha_{PE}$ and $\bar{\alpha}_y/\alpha_{PE}$ are a) equal and as negative as possible and b) both as close as possible to zero. The objective function and the evolution of the input parameters $\beta$ (blue line), $\delta$ (yellow line), and $a/b$ (purple line) are plotted against the iteration number. On the right, the optimized geometry is displayed in its deformed configuration and the values of the normalized thermal expansion coefficients are reported.

## Supporting Information

Supporting Information is available from the Wiley Online Library or from the author.

## Acknowledgements

This work was supported by the National Science Foundation under Grant No. DMR-1420570.

## Conflict of Interest

The authors declare no conflict of interest.

## Keywords

bilayer Miura-ori, extreme thermal expansion, metamaterials, origami, tunable thermal properties

[1] K. L. Chopra, P. D. Paulson, V. Dutta, *Prog. Photovolt.: Res. Appl.* **2004**, *12*, 69.
[2] W. Miller, C. W. Smith, D. S. Mackenzie, K. E. Evans, *J. Mater. Sci.* **2009**, *44*, 5441.
[3] K. Takenaka, *Sci. Technol. Adv. Mater.* **2012**, *13*, 013001.
[4] M. M. Toropova, C. A. Steeves, *Acta Astronaut.* **2015**, *113*, 132.
[5] M. R. Werner, W. R. Fahrner, *IEEE Trans. Ind. Electron.* **2001**, *48*, 249.
[6] N. Yamamoto, E. Gdoutos, R. Toda, V. White, H. Manohara, C. Daraio, *Adv. Mater.* **2014**, *26*, 3076.
[7] E. Gdoutos, A. A. Shapiro, C. Daraio, *Exp. Mech.* **2013**, *53*, 1735.
[8] R. Lakes, *J. Mater. Sci. Lett.* **1996**, *15*, 475.
[9] T.-C. Lim, *J. Mater Sci.* **2005**, *40*, 3275.
[10] C. A. Steeves, S. L. dos Santos e Lucato, M. He, E. Antinucci, J. W. Hutchinson, A. G. Evans, *J. Mech. Phys. Solids* **2007**, *55*, 1803.
[11] J. J. Lehman, R. S. Lakes, *Compos. Struct.* **2014**, *107*, 654.
[12] J. Qi, J. W. Halloran, *J. Mater. Sci.* **2004**, *39*, 4113.
[13] J. Qu, M. Kadic, A. Naber, M. Wegener, *Scientific Reports*, **2017**, *7*, 40643.
[14] Q. Wang, J. A. Jackson, Q. Ge, J. B. Hopkins, C. M. Spadaccini, N. X. Fang, *Phys. Rev. Lett.* **2016**, *117*, 175901.
[15] H. Xu, D. Pasini, *Sci. Rep.* **2016**, *6*, 34924.
[16] O. Sigmund, S. Torquato, *Appl. Phys. Lett.* **1996**, *69*, 3203.
[17] O. Sigmund, S. Torquato, *J. Mech. Phys. Solids* **1997**, *6*, 1037.
[18] M. Eidini, G. H. Paulino, *Sci. Adv.* **2015**, *1*, e1500224.
[19] C. Lv, D. Krishnaraju, G. Konjevod, H. Yu, H. Jiang, *Sci. Rep.* **2014**, *4*, 5979.
[20] M. Schenk, S. D. Guest, *Proc. Natl. Acad. Sci. USA* **2013**, *110*, 3276.
[21] Z. Y. Wei, Z. V. Guo, L. Dudte, H. Y. Liang, L. Mahadevan, *Phys. Rev. Lett.* **2013**, *110*, 215501.
[22] L. H. Dudte, E. Vouga, T. Tachi, L. Mahadevan, *Nat. Mater.* **2016**, *15*, 583.
[23] J. L. Silverberg, A. A. Evans, L. Mcleod, R. C. Hayward, T. Hull, C. D. Santangelo, I. Cohen, *Science* **2014**, *345*, 647.
[24] J. L. Silverberg, J.-H. Na, A. A. Evans, B. Liu, T. C. Hull, C. D. Santangelo, R. J. Lang, R. C. Hayward, I. Cohen, *Nat. Mater.* **2015**, *14*, 389.
[25] K. Miura, *The Institute of Space and Astronautical Science Report*, Vol. *618*, Institute of Space and Astronautical Science, Yoshinodai, Sagamihara, Kanagawa, Japan **1985**, p. 1.
[26] M. Danielsson, D. Parks, M. Boyce, *J. Mech. Phys. Solids* **2002**, *50*, 351379.
[27] F. S. Hillier, G. J. Lieberman, *Introduction to Operations Research*, 7th ed., McGraw Hill, New York **2001**.
[28] M. J. D. Powell, in *Advances in Optimization and Numerical Analysis* (Eds: S. Gomez, J.-P. Hennart), Kluwer Academic, Dordrecht, The Netherlands **1994**, p. 51.
[29] G. Jefferson, T. A. Parthasarathy, R. J. Kerans, *Int. J. Solids Struct.* **2009**, *46*, 2372.
[30] R. Bastaits, G. Rodrigues, Ph. Jetteur, P. Hagedorn, A. Preumont, *Smart Mater. Struct.* **2012**, *21*, 064004.
[31] K. Zweibel, *Sol. Energy Mater. Sol. Cells* **2000**, *63*, 375.
[32] C. Zweben, *JOM* **1998**, *50*, 47.


© 2017 WILEY-VCH Verlag GmbH & Co. KGaA, Weinheim

Copyright WILEY-VCH Verlag GmbH & Co. KGaA, 69469 Weinheim, Germany, 2017.

ADVANCED MATERIALS

# Supporting Information

for *Adv. Mater.*, DOI: 10.1002/adma.201700360

# Origami Metamaterials for Tunable Thermal Expansion

*Elisa Boatti, Nikolaos Vasios, and Katia Bertoldi**

# SUPPLEMENTAL MATERIALS

## Origami metamaterials for tunable thermal expansion

Elisa Boatti[1], Nikolaos Vasios[1] and Katia Bertoldi[1,2]*

[1]*John A. Paulson School of Engineering and Applied Sciences, Harvard University, Cambridge, MA 02138, USA and*

[2]*Kavli Institute, Harvard University, Cambridge, MA 02138, USA*

(Dated: March 20, 2017)

*Correspondence to bertoldi@seas.harvard.edu

# I. EXPERIMENTS

## A. Fabrication

The Miura-ori considered in this study were fabricated from paper (Boise ASPEN 30, 92 Brightness, 20lb, 11 x 17) and adhesive-backed UHMW (ultra-high molecular weight) polyethylene films (McMaster-Carr identification number 1441T12). As shown in Fig. S1, samples composed of $5 \times 5$ unit cells were manufactured by etching the creases pattern separately on the paper and on the polyethylene film with a laser cutter (*Versa Laser 2.0*). Then the polyethylene film was glued on top of the paper in the desired locations. Finally, the bilayer Miura-ori structures were manually folded.

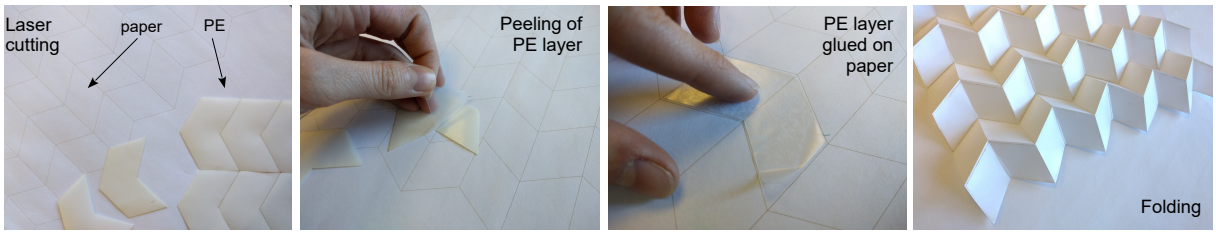


FIG. S1: **Fabrication of the Miura-ori structures.** From left to right: firstly the paper is etched and the polyethylene layers are cut using a laser cutter; secondly the polyethylene layers are peeled off the protective film and glued in appropriate locations on top of the paper; finally the structure is manually folded.

## B. Materials characterization

The Young's modulus of both the paper sheets and the polyethylene films was experimentally measured conducting tensile tests with an *Instron* model 5566 equipped with a 100 N load cell. We found that $E_{\text{paper}} = 4700$ MPa and $E_{\text{PE}} = 400$ MPa.

Finally, while for the thermal expansion coefficient of the paper we assumed $\alpha_{\text{paper}} = 2 \times 10^{-6}$ K$^{-1}$ [1], to characterize $\alpha_{\text{PE}}$ we measured the curvature $\kappa$ upon heating of a bilayer strip made of paper and polyethylene film. We then used the Timoshenko formula [5] to

obtain $\alpha_{\mathrm{PE}}$ as

$$\alpha_{\mathrm{PE}} = \alpha_{\mathrm{paper}} + \frac{\kappa}{\Delta T} \cdot \frac{h(3(1+m)^2 + (1+mn)(m^2 + \frac{1}{mn}))}{6(1+m)^2} \tag{S1}$$

where $\Delta T$ is the applied change in temperature, $m = t_{\mathrm{paper}}/t_{\mathrm{PE}}$, $n = E_{\mathrm{paper}}/E_{\mathrm{PE}}$ and $h = t_{\mathrm{paper}} + t_{\mathrm{PE}}$. We found $\alpha_{\mathrm{PE}} = 1.3 \times 10^{-4}$ K$^{-1}$, in accordance with the seller information.

### C. Creases stiffness

The stiffness for both the soft (only paper layer) and stiff (paper-polyethylene bilayer) creases was characterized experimentally by performing uniaxial tensile tests on a rectangular strip comprising three folds (see Fig. S2). The strips were tested using an *Instron* electromechanical testing system (model 5566) equipped with a 10 N load cell and imposing a gradual folding. The two ends of the strip were fixed as shown in Fig. S2 and the reaction force $F$ was monitored during folding. Assuming the creases act as torsional springs with stiffness $k_{\mathrm{crease}}$ per unit length, work balance yields

$$F\Delta u = 2(\xi_f - \xi_i)k_{\mathrm{crease}}w_f \tag{S2}$$

where $\Delta u$ is the displacement applied by the Instron, $\xi_i$ and $\xi_f$ are the initial and final opening angle of the crease, respectively, and $w_f$ denotes the width of the crease (see Fig. S2(a)). Note that $\xi_i$ and $\xi_f$ can be calculated as:

$$\xi_i = 2\arcsin\left(\frac{h_i}{l}\right), \quad \xi_f = 2\arcsin\left(\frac{h_i + \Delta u}{l}\right) \tag{S3}$$

where $h_i$ is the initial opening of the strip and $l$ denotes the length of the plates (see Fig. S2). Substitution of Eqs. (S3) into Eq. (S2), yields

$$k_{\mathrm{crease}} = \frac{F\Delta u}{4w_f\left[\arcsin\left(\frac{h_i + \Delta u}{l}\right) - \arcsin\left(\frac{h_i}{l}\right)\right]}. \tag{S4}$$

By using Eq. (S4) to calculate the stiffness of the creases from our experimental data, we found that $k_{\mathrm{crease}}$ varies noticeable among different samples. This is because the response of the creases is highly affected by the way they are manually folded - a process that is very difficult to precisely control. Moreover, we also found a certain degree of nonlinearity,

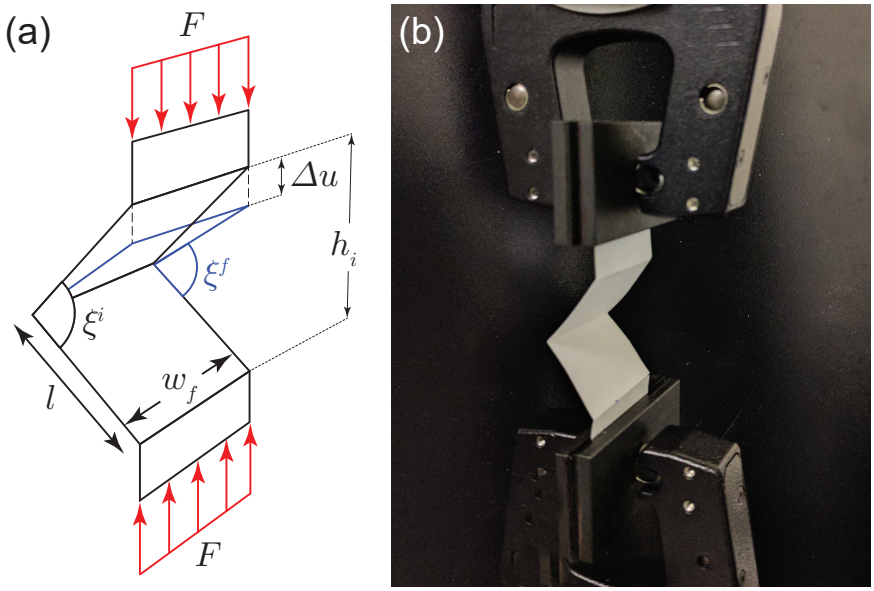


FIG. S2: **Creases stiffness measurement.** (a) Schematic of the fold. (b) Picture of the sample mounted on the *Instron*.

especially for small opening angles. For the sake of simplicity, we decided to approximate the response of the creases using linear torsional springs, therefore neglecting the deviation from linearity that the folds present upon varying opening angles. By averaging the results obtained from four tests per crease type, we found $k_{\text{soft}} = 0.0021 \pm 0.0003$ N/rad and $k_{\text{stiff}} = 0.0205 \pm 0.0055$ N/rad. As expected, stiff creases are one order of magnitude stiffer than the soft ones.

### D. Testing

To characterize the effective coefficients of thermal expansion of the proposed structures, we placed them in an oven (model 414004-580 VWR) and gradually increased the temperature, while monitoring the evolution of their projected area with a camera. The pictures were then analyzed by digital image processing (*Matlab*) and their contrast was digitally increased in order to clearly distinguish the creases.

For each experiment, we first focused on the picture at room temperature and calculated the opening angle $\delta$. To minimize the influence of edge effects, we focused on four unit cells in the center of the sample (highlighted by the red squares in Fig. S3). For each unit cell,

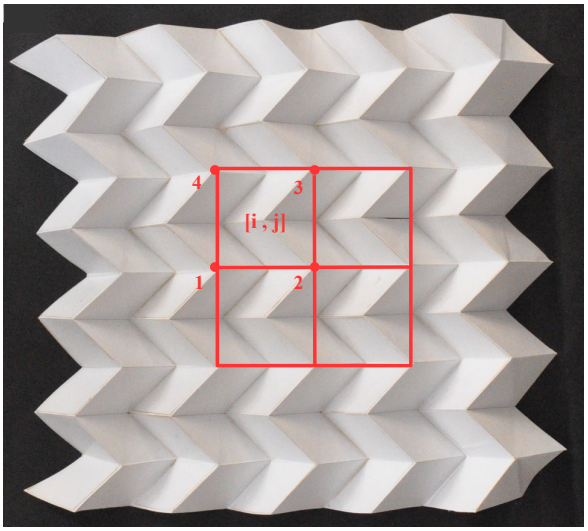


FIG. S3: **Digital image postptocessing.** Unit-cells used to calculate $\delta$, $\bar{\alpha}_x$ and $\bar{\alpha}_y$.

we calculated the opening angle as [4]

$$\delta^{[i,j]} = \pi - 2\arcsin\left(\frac{1}{\sin(\beta)}\sqrt{1-\frac{\left(L_x^{[i,j]}\right)^2}{4a^2}}\right),$$

where $L_x^{[i,j]}$ denotes the initial length of the $[i,\, j]$-th cell along $x$ direction,

$$L_x^{[i,j]} = \frac{\left(X_3^{[i,j]} - X_4^{[i,j]}\right) + \left(X_2^{[i,j]} - X_1^{[i,j]}\right)}{2}, \tag{S5}$$

$X_\gamma^{[i,j]}$ being the $x$ coordinate of the $\gamma$-th vertex of the cell in the undeformed configuration (see Fig. S3). Finally, the opening angle for the Miura-ori is obtained as

$$\bar{\delta} = \frac{1}{4}\sum_{i=1}^{2}\sum_{j=1}^{2}\delta^{[i,j]}. \tag{S6}$$

We then used the picture taken after heating to obtain $\bar{\alpha}_x$ and $\bar{\alpha}_y$. Again, to minimize the influence of edge effects, we focused on four unit cells in the center of the sample. For each unit cell, the elongation along the $x$ and $y$ directions, $\Delta x^{[i,j]}$ and $\Delta y^{[i,j]}$, were calculated from the position of the Miura-ori's vertices as

$$\begin{aligned}
\Delta x^{[i,j]} &= \frac{\left(x_3^{[i,j]} - x_4^{[i,j]} - X_3^{[i,j]} + X_4^{[i,j]}\right) + \left(x_2^{[i,j]} - x_1^{[i,j]} - X_2^{[i,j]} + X_1^{[i,j]}\right)}{2} \\
\Delta y^{[i,j]} &= \frac{\left(y_4^{[i,j]} - y_1^{[i,j]} - Y_4^{[i,j]} + Y_1^{[i,j]}\right) + \left(y_3^{[i,j]} - y_2^{[i,j]} - Y_3^{[i,j]} + Y_2^{[i,j]}\right)}{2}
\end{aligned} \tag{S7}$$

where $X_\gamma^{[i,j]}$, $Y_\gamma^{[i,j]}$ and $x_\gamma^{[i,j]}$, $y_\gamma^{[i,j]}$ are the $x$ and $y$ coordinates of the $\gamma$-th vertex for the cell $[i,j]$, in the undeformed and deformed configurations, respectively (see Fig. S3). For the $[i,\,j]$-th unit cell macroscopic values of the coefficient of thermal expansion were then obtained as

$$\begin{aligned} \alpha_x^{[i,j]} &= \frac{\Delta x^{[i,j]}}{L_x^{[i,j]}\,\Delta T}, \\ \alpha_y^{[i,j]} &= \frac{\Delta y^{[i,j]}}{L_y^{[i,j]}\,\Delta T}, \end{aligned} \tag{S8}$$

where $\Delta T$ is the change in temperature and $L_x^{[i,j]}$ is given by Eq. (S5) and $L_y^{[i,j]}$ denotes the initial length of the cell along $y$,

$$L_y^{[i,j]} = \frac{\left(Y_4^{[i,j]} - Y_1^{[i,j]}\right) + \left(Y_3^{[i,j]} - Y_2^{[i,j]}\right)}{2}. \tag{S9}$$

Finally, the ensemble average of the four central unit cells under consideration was computed,

$$\bar{\alpha}_x = \frac{1}{4}\sum_{i=1}^{2}\sum_{j=1}^{2}\alpha_x^{[i,j]}, \quad \bar{\alpha}_y = \frac{1}{4}\sum_{i=1}^{2}\sum_{j=1}^{2}\alpha_y^{[i,j]}. \tag{S10}$$

Lastly, we want to emphasize the fact that the response of the system is reversible and repeatable. In fact, upon cooling back to room temperature the component recovers the initial configuration. Therefore, numerous thermal tests can be performed on the same sample.

## II. NUMERICAL ANALYSIS

In order to investigate the response of the considered Miura-ori structures, implicit static analyses were performed using the software *Abaqus*/Standard (*Dassault Systèmes, Providence, RI*). The behavior of the system was simulated considering a unit cell with suitable periodic boundary conditions. The models were meshed using six nodes quadratic triangular shell elements (Abaqus element type STRI65) with a mesh element size equal to $(a+b)/120$. The bilayer plates were simulated as composite layups, composed of a paper and a polyethylene layer. The materials behavior was captured using linear elasticity, assigning the Young's moduli measured in Section I B and assuming the Poisson's ratio equal to 0.3 for both paper and polyethylene. Finally, isotropic thermal expansion was assumed for both

materials and the coefficients of thermal expansion reported in Section I B were assigned. The creases were modeled using pin constraints to connect every pair of neighboring nodes on neighboring plates. A torsional spring constraint was also applied to each pair of nodes, using spring-dashpot objects. The spring stiffness assigned to each pair of nodes, $k_{\text{node pair}}$, was determined as

$$k_{\text{node pair}} = \frac{k_{\text{crease}}\ w_c}{n_p} \tag{S11}$$

where $k_{\text{crease}}$ is either $k_{\text{soft}}$ or $k_{\text{stiff}}$ depending on the type of crease, $w_c$ is the width of the considered crease and $n_p$ is the number of nodes pairs on the considered crease. A uniform temperature change was applied to the whole model in an implicit simulation step and the evolution of the macroscopic strains $\bar{\epsilon}_{xx}$ and $\bar{\epsilon}_{yy}$ was monitored.

### A. Effect of material properties

While the Miura-ori considered in this study were fabricated from paper and adhesive polyethylene film, we also investigated numerically the effect of the material properties on $\bar{\alpha}$. To this end, we focused on design $\#B$ (see Fig. 1-c in the main text) with $a/b$=1, $\beta = 60$ deg and $\delta = 70$ deg and studied how the macroscopic coefficient of thermal expansion is affected by the thickness, stiffness and coefficients of thermal expansion of the individual layers. It is important to note that changes in the Young's modulus and thickness of the two layers alter the stiffness of the creases and, as a consequence, the response of our system. We assumed that the bilayer creases behave as linear rotational springs with stiffness [7]

$$k_{\text{stiff}} = k_{\text{top+bottom}} = C\,\overline{EI}\left(\frac{1}{t_{\text{top}} + t_{\text{bottom}}}\right)^{1/3} \tag{S12}$$

where $C$ is a parameter that relates bending of a flat panel and folding at creases and

$$\overline{EI} = \frac{E_{\text{top}}}{1-\nu_{\text{top}}^2}\left[\frac{t_{\text{top}}^3}{12} + t_{\text{top}} d_{\text{top}}^2\right] + \frac{E_{\text{bottom}}}{1-\nu_{\text{bottom}}^2}\left[\frac{t_{\text{bottom}}^3}{12} + t_{\text{bottom}} d_{\text{bottom}}^2\right] \tag{S13}$$

is the equivalent flexural rigidity of the bilayer. Moreover, $E_\gamma$, $\nu_\gamma$ and $t_\gamma$ ($\gamma$ = top, bottom) are the Young's modulus, Poisson't ratio and thickness of the $\gamma$-th layer and

$$d_{\text{top}} = t_{\text{bottom}} + \frac{t_{\text{top}}}{2} - y_{\text{neutral axis}}, \quad d_{\text{bottom}} = \frac{t_{\text{bottom}}}{2} - y_{\text{neutral axis}}, \tag{S14}$$

with the position of the neutral axis given by

$$y_{\text{neutral axis}} = \frac{\dfrac{t_{\text{bottom}}^2}{2} + t_{\text{top}}\dfrac{E_{\text{top}}}{E_{\text{bottom}}}\left(t_{\text{bottom}} + \dfrac{t_{\text{top}}}{2}\right)}{t_{\text{bottom}} + t_{\text{top}}\dfrac{E_{\text{top}}}{E_{\text{bottom}}}}. \tag{S15}$$

Note that for creases made of the bottom layer only, the stiffness of the rotational spring can be calculated from Eq. (S12) by setting $t_{\text{top}} = 0$, yielding

$$k_{\text{soft}} = k_{\text{bottom}} = C\,\frac{E_{\text{bottom}}}{1-\nu_{\text{bottom}}^2}\frac{t_{\text{bottom}}^3}{12}\left(\frac{1}{t_{\text{bottom}}}\right)^{1/3} \tag{S16}$$

In Fig. S4 we show how $k_{\text{stiff}}/k_{\text{soft}}$ depends on the contrast in stiffness and thickness between the two layers (i.e. on $E_{\text{top}}/E_{\text{bottom}}$ and $t_{\text{top}}/t_{\text{bottom}}$), assuming $\nu_{\text{top}} = \nu_{\text{bottom}}$. As expected, we find that in the absence of the top layer (i.e. for $t_{\text{top}} = 0$ or $E_{\text{top}} = 0$) $k_{\text{stiff}}/k_{\text{soft}} = 1$ and that, as the contrast in properties between the two layers increases, $k_{\text{stiff}}/k_{\text{soft}}$ increases.

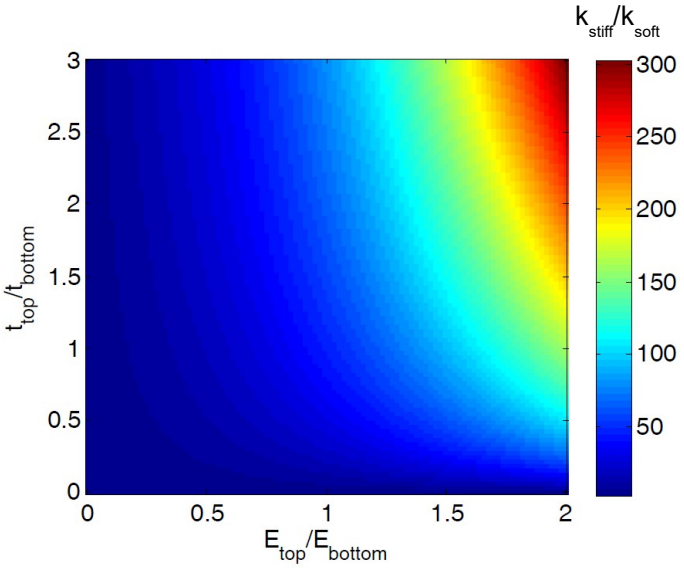


FIG. S4: **Crease stiffness.** Effect of $E_{\text{top}}/E_{\text{bottom}}$ and $t_{\text{top}}/t_{\text{bottom}}$ on the crease stiffness of a bilayer fold.

Having determined the effect of the Young's modulus and thickness of the two layers on the stiffness of the creases, we then investigated how the thermal expansion coefficients of

design $\#B$ is affected by changes in material properties and thicknesses. To this end, for each set of geometric (i.e. $t_{\text{top}}$ and $t_{\text{bottom}}$) and material (i.e. $E_{\text{top}}$, $\alpha_{\text{top}}$ and $E_{\text{bottom}}$, $\alpha_{\text{bottom}}$) parameters, we calculated the stiffness of the stiff and soft creases using Eqs. (S12) and (S16), respectively. To extract $\bar{\alpha}_x$ and $\bar{\alpha}_y$, we then conducted a FE simulation on a unit cell with the appropriate geometric and material parameters and values of $k_{\text{stiff}}$ and $k_{\text{soft}}$.

In Fig. S5 we report as contour plots the evolution of $\alpha_x$ and $\alpha_y$ (normalized by $\alpha_{\text{bottom}}$) as a function of $\alpha_{\text{top}}/\alpha_{\text{bottom}}$ and $E_{\text{top}}/E_{\text{bottom}}$ for three different cases. First, we considered $t_{\text{top}}/t_{\text{bottom}} = 1.27$ (as in our experiments) and $C = C_{\text{soft}} = 0.002$ and $C = C_{\text{stiff}} = 0.01$ in Eqs. (S12) and (S16). Note that this values of $C$ were chosen to best fit the experimentally measured values of $k_{\text{soft}}$ and $k_{\text{stiff}}$. Then, we assumed $t_{\text{top}}/t_{\text{bottom}} = 3$ and $C = C_{\text{soft}} = 0.002$ and $C = C_{\text{stiff}} = 0.01$. Finally, we chose $t_{\text{top}}/t_{\text{bottom}} = 1.27$ (as in our experiments) and $C = C_{\text{soft}} = 0.02$ and $C = C_{\text{stiff}} = 0.1$. The results reported in Fig. S5 show that for all three cases the thermal expansion coefficients of the Miura-ori are highly sensitive to the ratio $\alpha_{\text{top}}/\alpha_{\text{bottom}}$ and become more negative as the ratio increases. Differently, the ratio $E_{\text{top}}/E_{\text{bottom}}$ is found to have a more limited effect on $\bar{\alpha}_x$ and $\bar{\alpha}_y$. Moreover, as expected, our results indicate that the absolute value of $\bar{\alpha}_x$ and $\bar{\alpha}_y$ decreases as $t_{\text{top}}/t_{\text{bottom}}$ and the coefficients $C$ increase. This is because in these cases the bendability of the plates and deformability of the creases is reduced.

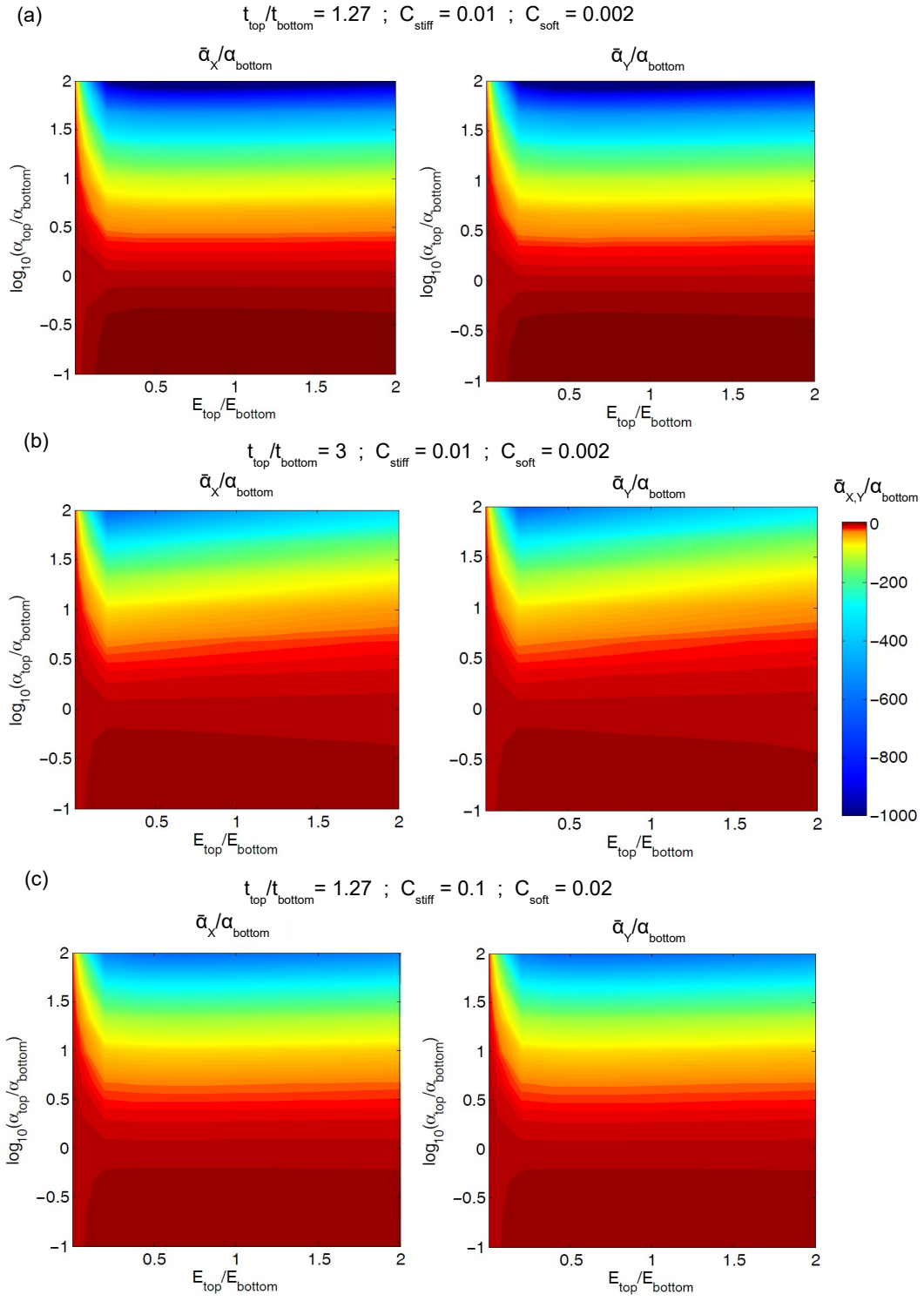


FIG. S5: **Effect of material parameters and layers thickness.** Evolution of $\bar{\alpha}_x$ and $\bar{\alpha}_y$ (normalized by $\alpha_{\text{bottom}}$) as a function of $\alpha_{\text{top}}/\alpha_{\text{bottom}}$ and $E_{\text{top}}/E_{\text{bottom}}$ for three different cases.

## B. Additional numerical results

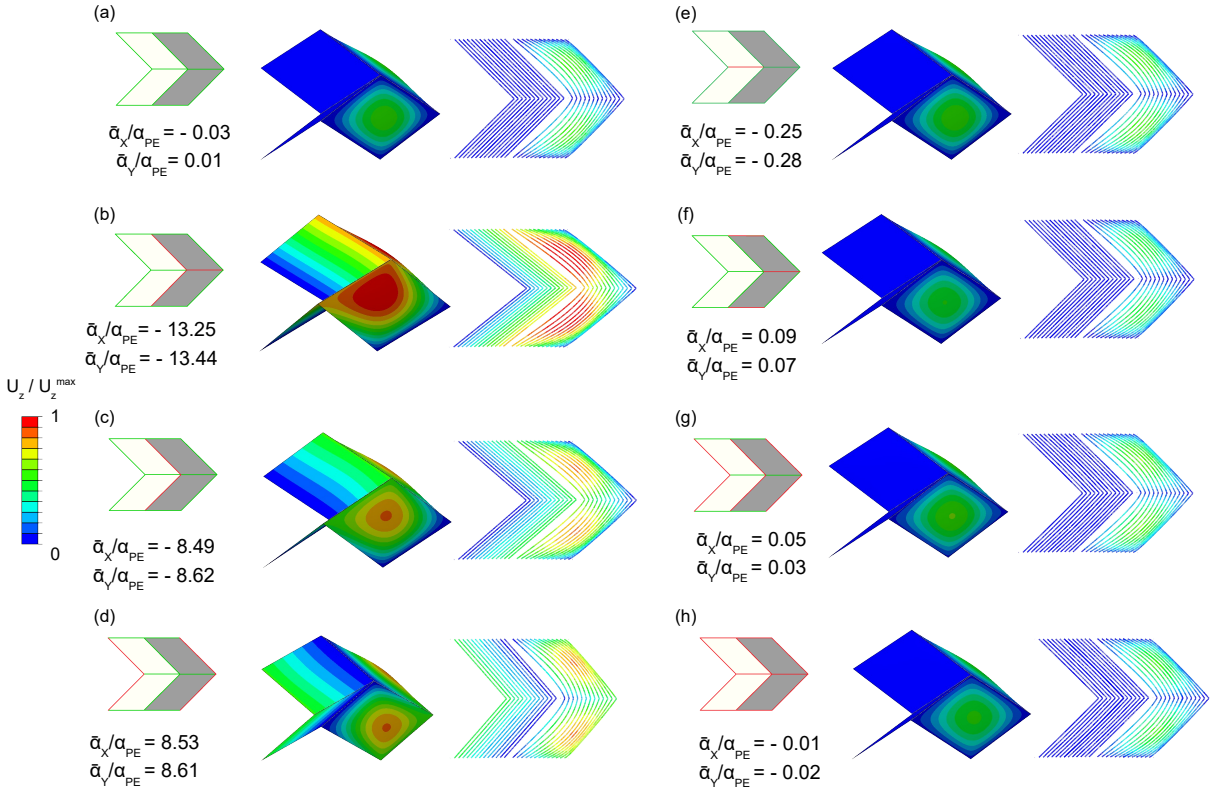


FIG. S6: **Effect of the arrangement of soft and stiff creases.** Response upon an increase in temperature for 8 different arrangements of soft and stiff creases. For each case the arrangement of the creases is shown on the left (green and red lines correspond to soft and stiff creases, respectively). Both rotated (left) and top (right) views are shown. The contours show the normalized displacement in z-direction. The values of $\bar{\alpha}_x/\alpha_{\mathrm{PE}}$ and $\bar{\alpha}_y/\alpha_{\mathrm{PE}}$ are also reported.

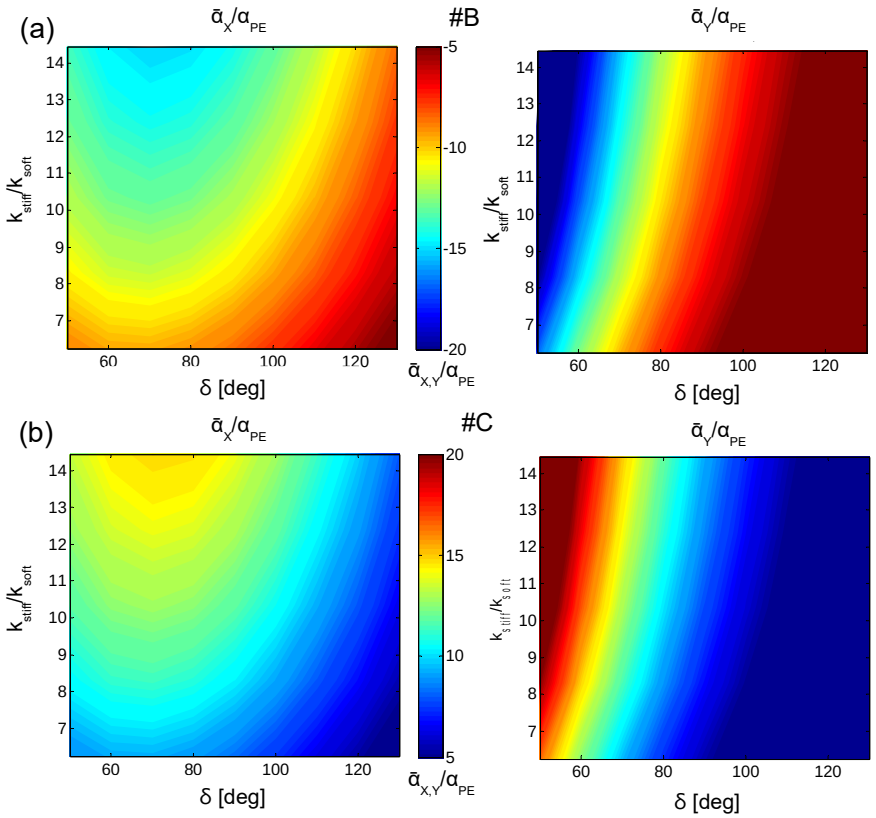


FIG. S7: **Effect of $k_{\mathbf{stiff}}/k_{\mathbf{soft}}$ and $\delta$ on $\bar{\alpha}_x$ and $\bar{\alpha}_y$.** Evolution of $\bar{\alpha}_x$ and $\bar{\alpha}_y$ as a function of $k_{\text{stiff}}/k_{\text{soft}}$ and $\delta$ for design (a) $\#B$ and (b) $\#C$. Note that these results are also included in Fig. 2 of the main text.

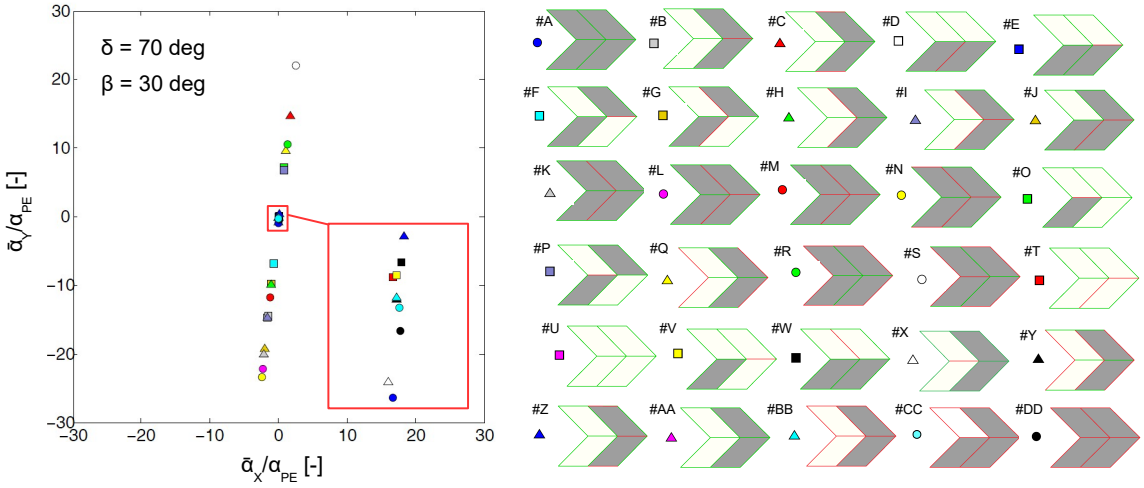


FIG. S8: **Effect of $\beta$ on the ratio $\bar{\alpha}_y/\bar{\alpha}_x$.** Numerical predictions for $\bar{\alpha}_x$ and $\bar{\alpha}_y$ for different arrangements of the bilayer plates and the soft and stiff creases, assuming $a/b = 1$, $\delta = 70$ deg and $\beta = 30$ deg. We find that for this particular choice of geometric parameters $\bar{\alpha}_y/\bar{\alpha}_x = 9.5$.

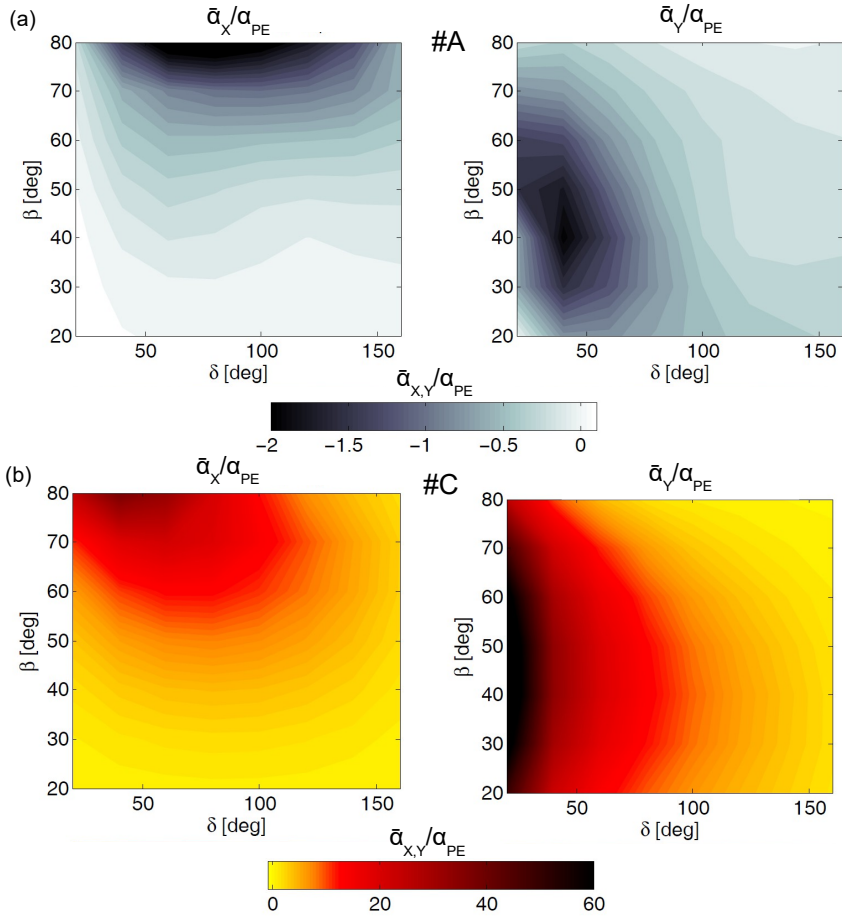


FIG. S9: **Effect of angles $\beta$ and $\delta$.** In Fig. 4 of the main text we present contour plots showing the evolution of of $\bar{\alpha}_x/\alpha_{\rm PE}$ (left) and $\bar{\alpha}_y/\alpha_{\rm PE}$ (right) as a function of the angles $\beta$ and $\delta$ for design $\#B$ (for $a/b = 1$). Here, we show such contour plots also for designs (a) $\#A$ and (b) $\#C$.

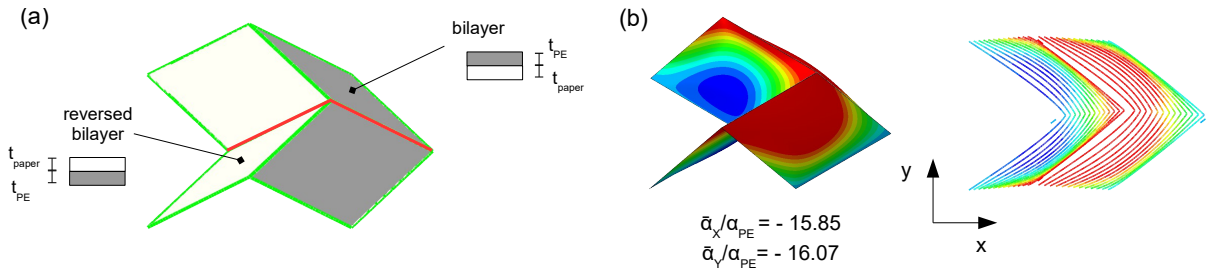


FIG. S10: **Effect of the bilayers orientation.** In this study we considered origami structures comprising single-layer plates made of paper and bilayer plates with paper on the bottom and polyethylene on the top. However, it is worth noting that the study can be further extended by introducing also bilayers with paper on the top and polyethylene on the bottom. To demonstrate this possibility, here we consider design $\#B$ and replace the single-layer faces with bilayer faces having paper on the top and polyethylene on the bottom and connected by a stiff crease. For a Miura-ori characterized by $a/b = 1$, $\beta = 60°$, and $\delta = 70°$ we find that $\bar{\alpha}_x/\alpha_{\rm PE} = -15.85$ and $\bar{\alpha}_y/\alpha_{\rm PE} = -16.07$. Note that these coefficients of thermal expansion are more negative than those presented in the main text for the same structure, demonstrating the benefits of the introduction of bilayers with opposite orientation.

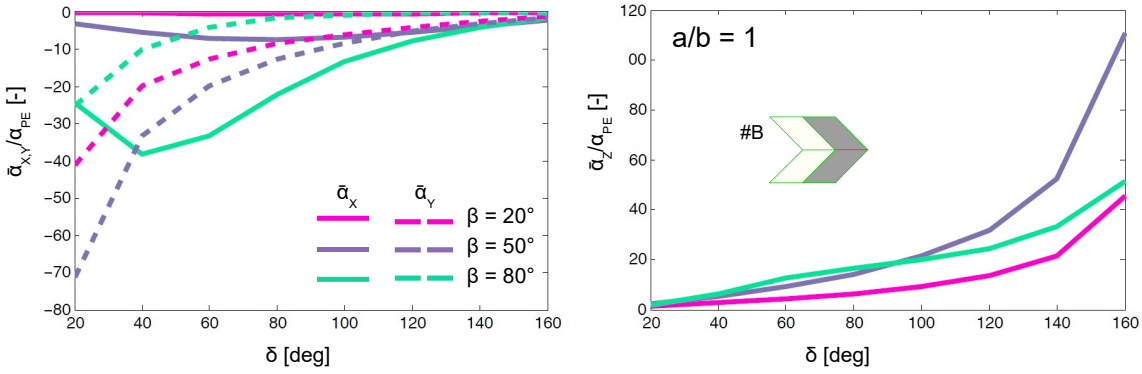


FIG. S11: **Coefficient of thermal expansion in $z$-direction.** While in the main text we focused on $\bar{\alpha}_x$ and $\bar{\alpha}_y$, here we also report $\bar{\alpha}_z$ for design $\#B$ with $a/b = 1$. Numerical predictions are reported for $\beta = 20, 50$, and $80°$ and for $\delta \in [20°, 160°]$. As expected, when the the Miura-ori shrinks in-plane, it expands along the $z$-direction.

## III. OPTIMIZATION

In an effort to identify Miura-ori configurations resulting in specific values of coefficients of thermal expansion, we used Python [3] and the COBYLA [2] optimization algorithm. In particular, we defined an objective function $\mathcal{Z}$ in terms of the in-plane thermal expansion coefficients $\bar{\alpha}_x$ and $\bar{\alpha}_y$, whereas the input parameters to that objective function were taken to be the acute angle $\beta$, the opening angle $\delta$ and the ratio of lengths of the parallelogram facets $a/b$. It is important to note that the arrangement of plates and creases was decided independently for each optimization and was assumed to be fixed throughout the optimization procedure. This allows for continuous but constrained optimization, where the constraints are introduced to ensure that any accessible point $\boldsymbol{P} = \{\beta, \delta, a/b\}$ corresponds to a well-defined Miura-ori shape. Guided by our simulations we constrained the optimization variables to lie in the intervals $\beta \in [10°, 90°]$, $\delta \in [20°, 160°]$ and $(a/b) \in [0.2, 2]$. Moreover, in order to ensure that all the variables in the optimization have similar orders of magnitude, we introduced the normalized geometric variables $\hat{\beta}, \hat{\delta}, \widehat{(a/b)}$

$$\hat{\beta} = \frac{\beta - 10°}{90° - 10°} \quad , \quad \hat{\delta} = \frac{\delta - 20°}{160° - 20°} \quad , \quad \widehat{(a/b)} = \frac{(a/b) - 0.2}{2 - 0.2} \tag{S17}$$

where now $\hat{\beta}, \hat{\delta}, \widehat{(a/b)}$ can only take values in the interval $[0, 1]$ as long as the following constraints are not violated,

$$g_1(\hat{\beta}) = 0.5 - \left|\hat{\beta} - 0.5\right| \geq 0 \tag{S18}$$

$$g_2(\hat{\delta}) = 0.5 - \left|\hat{\delta} - 0.5\right| \geq 0 \tag{S19}$$

$$g_3(\widehat{(a/b)}) = 0.5 - \left|\widehat{(a/b)} - 0.5\right| \geq 0 \tag{S20}$$

Therefore, the optimization problem can be formally introduced in the following form,

$$\text{Min } \mathcal{Z}_{(\text{i})} \quad , \quad i = a, b \tag{S21}$$

$$\text{s.t. } g_j(\hat{\boldsymbol{P}}) \geq 0 \quad , \quad j = 1, 2, 3$$

where $\hat{\boldsymbol{P}} = \{\hat{\beta}, \hat{\delta}, \widehat{(a/b)}\}$. The fact that the objective functions are defined in terms of the thermal expansion coefficients but the optimization has to be performed with respect to the normalized geometric parameters $\hat{\boldsymbol{P}}$ implies that for every evaluation of the objective function, a finite element simulation has to be performed [8]. This, in turn, entails that

there is no natural definition of a gradient of the objective function with respect to the optimization variables: therefore a fast, gradient free optimization algorithm had to be used which could also handle inequality constraints in the form of (S18-S20). The COBYLA [2] optimization algorithm, which is part of the *scipy* optimization module in Python, was a great fit for this problem being a gradient free algorithm that uses linear approximations to the objective and constraint functions and is suitable for nonlinear constrained optimization problems with low-dimensionality.

For every iteration of the COBYLA algorithm, a candidate for the optimal solution is obtained by solving the approximated linear programming problem [2]. Then, the original objective and constraint functions are being used to yield a new data point in the optimization space. The trust region for the optimization has the form of a simplex whose relative size is determined by an independent, automatically tuned parameter $\rho$. Whenever the algorithm is unable to provide significant improvements to the objective function, the trust region is reduced by shrinking the simplex, thus refining the search. The optimization is assumed to have converged when the parameter $\rho$ which determines the simplex size reaches a limiting value $\rho_{\min}$ which is defined by the user.

### A. Objective functions

In Fig. 5 of the main text we report results for two different cases that are of great interest for applications: $(a)$ we determined the optimal Miura-ori geometry resulting in the most negative pair of identical coefficients of thermal expansion (i.e. we were looking for most negative pair of $\bar{\alpha}_x, \bar{\alpha}_y$ that simultaneously satisfies the condition $\bar{\alpha}_x = \bar{\alpha}_y$); (b) we are interested in a Miura-ori geometry characterized by $|\bar{\alpha}_x| = |\bar{\alpha}_y| \sim 0$. The objective functions for these two cases were defined in terms of the normalized in-plane coefficients of thermal expansion $\bar{\alpha}_x$ and $\bar{\alpha}_y$ as follows,

$$\mathcal{Z}_{(\mathrm{a})} = \frac{\bar{\alpha}_x + \bar{\alpha}_y}{1 + 0.5\,|\bar{\alpha}_x - \bar{\alpha}_y|} \tag{S22}$$

$$\mathcal{Z}_{(\mathrm{b})} = -\left[\,|\bar{\alpha}_x| + |\bar{\alpha}_y| + 10^8\left(\bar{\alpha}_x^2 - \bar{\alpha}_y^2\right)^2\,\right]^{-1/4} \tag{S23}$$

A contour plot of the objective functions defined in (S22) and (S23) is shown in Fig. S12. The function $\mathcal{Z}_{(\mathrm{a})}$ was chosen so that it is minimized when $\bar{\alpha}_x$, $\bar{\alpha}_y$ are both as negative

as possible and as equal as possible. The denominator in Eq. ((S22)) serves to penalize solutions for which the coefficients of thermal expansion are not equal. On the other hand, function $\mathcal{Z}_{(\mathrm{b})}$ has a global minimum when $\bar{\alpha}_x = \bar{\alpha}_y = 0$ in the form of divergence to negative infinity. This ensures that the optimization will converge to configurations for which the in-plane coefficients of thermal expansion are as close to zero as possible. Furthermore, the term $10^8 \left(\bar{\alpha}_x^2 - \bar{\alpha}_y^2\right)^2$ in Eq. ((S23)) penalizes configurations for which $\bar{\alpha}_x \neq \bar{\alpha}_y$ and vanishes only when $\bar{\alpha}_x = \pm\bar{\alpha}_y$.

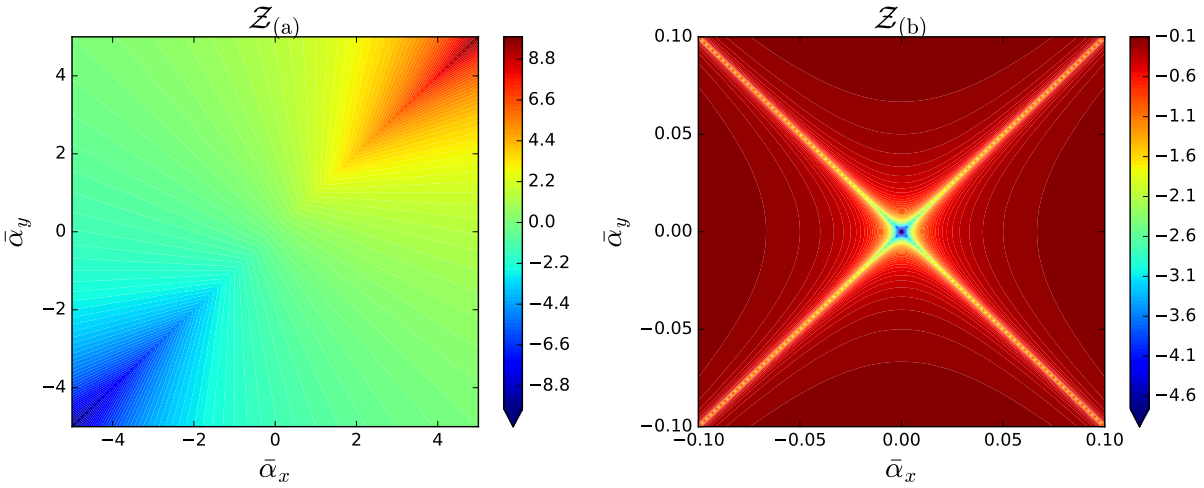


FIG. S12: **Objective Functions for Optimization** Contour plots of the objective functions $\mathcal{Z}_{(\mathrm{a})}$, $\mathcal{Z}_{(\mathrm{b})}$ chosen to achieve (a) equal negative and (b) both zero coefficients of thermal expansion.


[1] J. Borch, M. B. Lyne, R. E. Mark, C. Habeger. Handbook of Physical Testing of Paper: Volume 2. **2001**, *CRC Press*.

[2] M. J. D. Powell. A direct search optimization method that models the objective and constraint functions by linear interpolation. *Advances in Optimization and Numerical Analysis*, **eds.** S. Gomez and J-P Hennart, Kluwer Academic (Dordrecht),**1994**, 51–67

[3] G. van Rossum and F.L. Drake (eds). Python Reference Manual, PythonLabs, Virginia, USA, **2001**. Available at http://www.python.org

[4] M. Schenk, S. D. Guest. Geometry of Miura-folded metamaterials. *PNAS*, **2013**, 110(9), 3276–3281.

[5] S. Timoshenko. Analysis of Bi-Metal Thermostats. *Journal of the Optical Society of America*, **1925**, 11(3):233.

[6] Z. Y. Wei, Z. V. Guo, L. Dudte, H. Y. Liang, L. Mahadevan. Geometric Mechanics of Periodic Pleated Origami. *PRL* **2013**, 110, 215501.

[7] E.T. Filipov, T. Tachi, G.H. Paulino. Origami tubes assembled into stiff, yet reconfigurable structures and metamaterials. *Proceedings of the National Academy of Sciences* **2015**, 112, 12321-12326.

[8] For every choice of $\hat{\beta}, \hat{\delta}, \widehat{(a/b)}$, we determined the thermal response of the Miura-Ori unit-cell as described in section II and evaluated the objective function using the $\bar{\alpha}_x$ and $\bar{\alpha}_y$ that correspond to that simulation.